

# Analysis and Experimental Investigation of High-Frequency Magnetic Flux Distribution in Mn-Zn Ferrite Cores

Marcin Kački<sup>1</sup>, Marek S. Ryłko<sup>1</sup>, *Member, IEEE*, John G. Hayes<sup>2</sup>, *Senior Member, IEEE*, and Charles R. Sullivan, *Fellow, IEEE*

**Abstract**— This article presents a comprehensive investigation of the high-frequency magnetic flux distributions in manganese-zinc ferrite ring cores. New experimental characteristics are presented and used in the flux modeling. The flux distribution is predicted by a one-dimensional analytical model, a transmission-line model, and finite-element analysis. The models are used to investigate the high-frequency effects, such as skin depth and dimensional resonance. A complete experimental validation is presented. The nonuniform magnetic flux distributions are experimentally validated for two Mn-Zn materials: 3F36 and 3E10. The low permeability 3F36 material performance can be significantly degraded by dimensional resonance. However, the high permeability 3E10 material degrades due to the skin effect. The presented analytical methods show a very good correlation with the measurements.

**Index Terms**—Electromagnetic modeling, ferrite, finite-element analysis, magnetic materials, permeability, permittivity.

## I. INTRODUCTION

THE continuous drive for improvement of power electronic energy conversion is focusing on higher switching frequencies, which allows for system size and cost reduction, while still providing high efficiency. This technology development demands new solutions and fosters an interest into new wide-band-gap semiconductors with superior switching performance over the traditional silicon-based power semiconductors [1], [2], [3], [4]. This shift to higher switching frequencies creates a challenge for magnetic component design. The combination of relatively high permeability and moderate losses found in

manganese-zinc (Mn-Zn) ferrites makes them attractive for electromagnetic interference (EMI) filtering in the frequency range of kilohertz to megahertz. However, at high frequency the high permeability and high permittivity of the Mn-Zn ferrite cores may lead to skin and dimensional-resonance effects, which can cause nonuniform magnetic flux distribution in the core cross-section and degrade filter performance [5]. Both eddy-current and dimensional-resonance phenomena have been known from a fields perspective for many years. Previous work shows that the combination of dimensional resonance and eddy-currents in ferrite cores increases the core loss and thereby decreases the efficiency of the device [6].

Additionally, inductors and transformers do not scale well with frequency, not only due to efficiency and power dissipation constraints, but also due to the skin effect and dimensional resonance. Magnetic core performance is dictated by the variation of the permittivity and permeability characteristics with frequency [7], [8]. Often magnetic components are custom designs based on the available material information. Generally, the ferrite manufacturers' specifications provide average material characteristics, which may be of limited use for detailed analysis. The relatively poor quality of the material data can jeopardize an efficient design process for high-power and high-frequency magnetic components. Therefore, high fidelity characteristics of magnetic materials are required [9], [10].

The fundamental work on flux distribution analysis presented in [10], [11], and [13] was mainly focused on magnetic material complex characteristics measurements and their impact on magnetic flux distribution. The related presented magnetic flux distribution is based on the finite element analysis (FEA) simulations only. Additionally, reports by the authors for the power supply manufacturers association [12], [13] discuss a novel methodology for experimental flux validation. The novelties of this article are in the introduction of the shell-based transmission-line model (TLM) for core analysis, in the development of a novel experimental method to observe the flux distribution in the core, and a comparison with widely-used FEA and one-dimensional (1-D) models using high-fidelity experimental data.

Once the performance of the material is known, the next step is to develop specific models to provide high quality physical phenomena prediction. However, there is limited literature showing the critical parameter variation with frequency and the related modeling. Therefore, a detailed knowledge and related

Manuscript received 25 February 2022; revised 12 May 2022 and 15 July 2022; accepted 9 August 2022. Date of publication 23 August 2022; date of current version 10 October 2022. Recommended for publication by Associate Editor M. Chen. This paper is an extension of work presented in APEC 2019 [DOI: 10.1109/APEC.2019.8722252], APEC 2020 [DOI: 10.1109/APEC39645.2020.9124101], and PSMA reports [12],[13]. A companion paper on the related measurements methods has also been submitted to IEEE TPEL [DOI: 10.1109/TPEL.2022.3189671]. (*Corresponding author: John G. Hayes.*)

Marcin Kački and Marek S. Ryłko are with the R&D SMA Magnetics sp. z o.o., 32-085 Modlniczka, Poland (e-mail: marcin.kacki@sma-magnetics.com; marek.rylko@sma-magnetics.com).

John G. Hayes is with the School of Engineering, University College Cork, T12 K8AF Cork, Ireland (e-mail: john.hayes@ucc.ie).

Charles R. Sullivan is with the Thayer School of Engineering, Dartmouth College, Hanover, NH 03755 USA (e-mail: charles.r.sullivan@dartmouth.edu). Color versions of one or more figures in this article are available at <https://doi.org/10.1109/TPEL.2022.3200954>.

Digital Object Identifier 10.1109/TPEL.2022.3200954

analytical interpretation of the magnetic materials' performance over frequency and physical size are key to a successful design.

This article presents a detailed analysis of the magnetic flux distributions in Mn-Zn ferrite ring cores based on the complex material characteristics, which are generated experimentally by the authors. Three calculation methods to determine the magnetic flux distributions are presented, analyzed and contrasted. Section II presents the experimental results for the real and imaginary permeability and permittivity for two different Mn-Zn ferrite materials. Section III outlines a 1-D model capturing the impact of skin depth and dimensional resonance on magnetic flux distribution. Section IV discusses a novel, intuitive shell-based TLM. Section V shows the results of a magnetic flux analysis based on the earlier approaches as FEA. Section VI shows, the novel experimental validation results of magnetic flux distribution. Conclusion is presented in Section VII. Appendix II presents the permeability and permittivity characteristics of the two materials obtained experimentally.

## II. HIGH FREQUENCY ELECTRICAL PROPERTIES OF MN-ZN FERRITES

Complex permeability and permittivity are essential parameters to characterise magnetic materials, especially for EMI applications. New experimental characterizations of these parameters are presented in this section.

### A. Core Complex Permeability

The complex permeability is expressed by its real (reactive) component  $\mu'$  and imaginary (dissipative) component  $\mu''$ . The complex impedance  $\bar{Z}$  can be represented by the series model based on complex permeability

$$\bar{Z} = j\omega L_S + R_S = j\omega L_0 (\mu'_S - j\mu''_S) \quad (1)$$

where  $R_S$  and  $L_S$  are the series resistance and the series inductance, respectively,  $L_0$  is the inductance of the core with unity permeability,  $\omega$  is the angular frequency,  $j$  is the complex operator, and  $\mu'$  and  $\mu''$  are the absolute value of real and imaginary permeabilities in the series model.

The material complex permeability has been experimentally investigated by the authors by using a number of size samples to eliminate the core size effect [9], [10]. Depending on the test frequency, the physical dimensions of the Mn-Zn ferrite samples can significantly affect the measured core permeability characteristics. In order to minimize the measurement distortion due to a relatively large physical size, the selected core should have the smallest dimensions possible. Thus, the toroidal core T6/4/2.8 was selected as the smallest appropriate core available on the market. This core comes directly from the manufacturing press and has been sintered without further mechanical processing, such as polishing, grinding, etc. Additional mechanical processing needs to be avoided in order to preserve the material properties. The measurement requires a purpose-built cup-shaped test fixture coupled with a Wayne Kerr 6550B analyzer [14]. Thus, the resulting permeability characteristic provides the material data for the highest possible accuracy for further calculations.

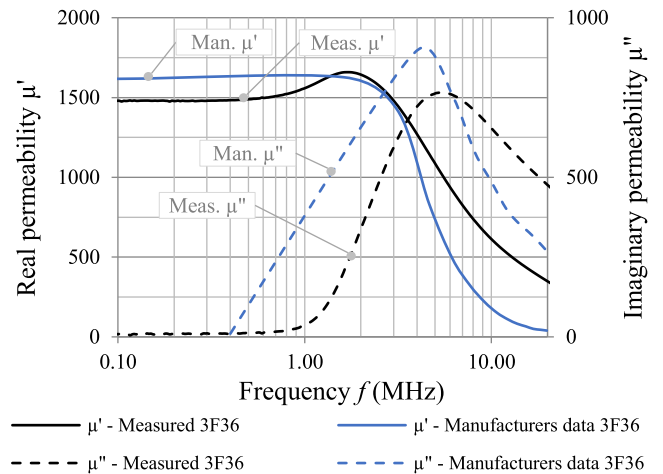


Fig. 1. Complex permeability versus frequency of 3F36 ferrite based on experimental and manufacturers data.

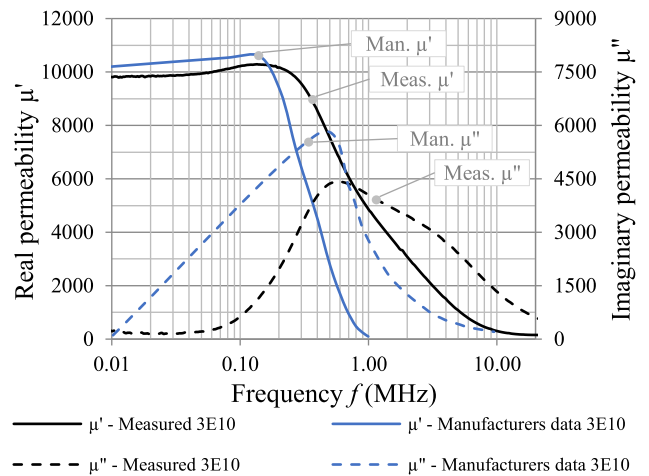


Fig. 2. Complex permeability versus frequency of 3E10 ferrite based on experimental and manufacturers data.

Two materials, 3F36 and 3E10, were selected for the flux distribution analysis. Permeability and permittivity values for the selected materials shows the contrast in the Mn-Zn ferrite group, i.e., low permeability and permittivity for 3F36 and high permeability and permittivity for 3E10. Such material selection emphasizes the skin and dimensional resonance effects. The flux distribution for a low permeability and permittivity material, such as 3F36, is dominated by dimensional resonance. In contrast a high permeability and permittivity material, such as 3E10, is dominated by skin effect. Plots of real  $\mu'$  and imaginary permeability  $\mu''$  for 3F36 and 3E10 materials are shown in Figs. 1 and 2, respectively.

In this article, we are distinguishing between the intrinsic and apparent permeabilities. For example the permeabilities presented in Figs. 1 and 2, are the intrinsic permeabilities. The later experimentally-measured permeabilities are apparent permeabilities. The word apparent is used because the measured permeability values can be significantly affected by the core high-frequency effects, such as permittivity and core loss.

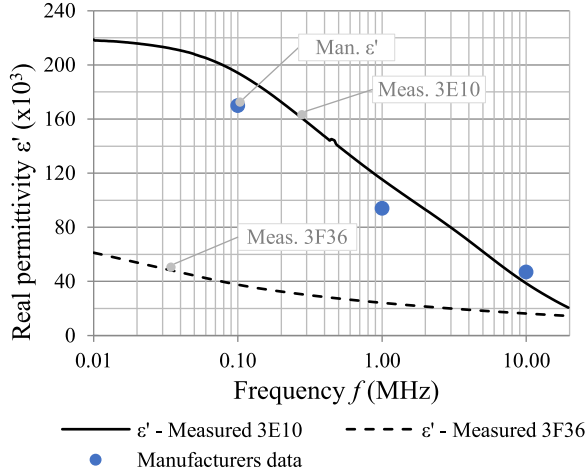


Fig. 3. Real permittivity versus frequency characteristic based on experimental data for Ferroxcube 3E10 and 3F36.

The characteristics were measured for a toroidal core with an external diameter of 6 mm, an inner diameter of 4 mm and a 2.8 mm height. As can be seen in the figures, the measured complex permeability characteristics vary with frequency and significantly differ from data provided in the manufacturer's specification, especially for frequencies above 1 MHz. This measured data is used for all the flux distribution calculations in this article.

### B. Core Complex Permittivity

In order to define the ferrite electrical characteristics for the dielectric constant  $\epsilon$  and conductivity  $\sigma$ , a dedicated test fixture was developed as discussed in [11]. Kaçki et al. [11] also shows the impact of the specific measurement condition, such as sample size, temperature and force, on ferrite complex permittivity. The dielectric properties of the 3E10 and 3F36 ferrites, which are used for the calculation in the next sections, were measured on solid cylindrical cores (external diameter 1.8 mm, height 18 mm). The obtained data has been extrapolated to 20 MHz with the constant-phase elements (CPEs) to eliminate high frequency effects. The measured complex permittivity characteristics for the smallest sample can be significantly affected by the dimensional resonance at certain frequencies. However, the dimensional resonance effect can be eliminated by using an equivalent CPE circuit to extrapolate the measurements [11]. The equivalent circuit assumes that the extracted parameters are examined at frequencies where the frequency effects are not present, enabling the extrapolation of the core behavior, as explained in [11]. The test method is validated up to 5 MHz, as the physical sample size is small. The characteristics are then extrapolated from 5 MHz upward. The real part of the permittivity frequency characteristics for 3E10 and 3F36 material are shown in Fig. 3, while the imaginary part of the permittivity frequency characteristics for 3E10 and 3F36 material are shown in Fig. 4.

The 3E10 material has the highest dielectric constant. The real permittivity of the 3F36 is one fifth of the 3E10 real permittivity. Thus, the material datasheets that provide common parameters

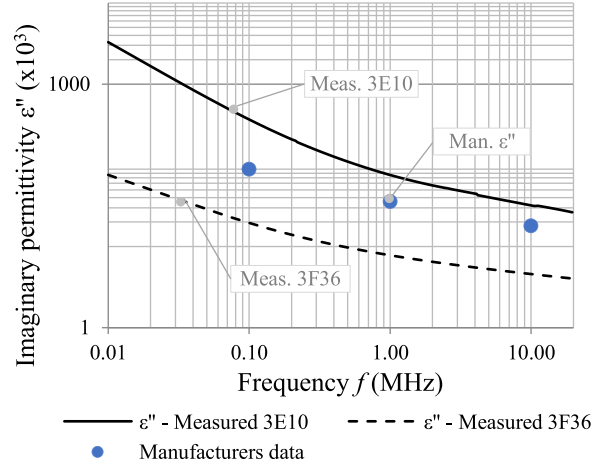


Fig. 4. Imaginary permittivity versus frequency characteristic based on experimental data for Ferroxcube 3E10 and 3F36.

for all Mn-Zn ferrites, and without details of the frequency dependence, are of limited benefit [15].

The imaginary permittivity frequency characteristics of the tested samples in the low-frequency region is determined by the grain boundary resistivity and has a very high value. At higher frequencies, the grain boundary resistance is shunted by the capacitance of the boundary, thus the observed bulk imaginary permittivity decreases with frequency. We also note that the eddy-current loss calculations based on the typical manufacturers datasheet may also result in significant estimation error [10]. The effect is magnified for large ferrite cores, where eddy-current losses are significant.

### III. SKIN DEPTH AND DIMENSIONAL RESONANCE

Ferrites have high permittivity and permeability. Therefore, the electromagnetic waves entering the ferrite propagate slower than in free space, or equivalently, the wavelength in the ferrite is shorter than in free space [16], [17]. The wave speed  $v$ , the frequency  $f$ , and the wavelength  $\lambda$  are related by

$$f = \frac{v}{\lambda}. \quad (2)$$

As a consequence any wave entering the ferrite changes its speed and wavelength. The wave that is propagating through the ferrite is damped due to material losses. A visualization of a wave propagating through a lossy material is shown in Fig. 5.

The skin depth is defined as the equivalent depth that the electromagnetic wave can penetrate the material by a factor of  $e^{-1}$  [16].

In low-loss materials, the electromagnetic wave travels without significant energy loss. If the smallest core cross-sectional dimension perpendicular to the magnetic and electric fields is equal to half a wavelength  $\lambda/2$ , then a standing wave will be set up across the core cross section. For this condition the surface flux, which is in phase with the surface magnetic field, is cancelled by antiphase flux at the core centre. This phenomena is called dimensional resonance and it is characterized by the permeability dropping to zero. The dimensional resonance and

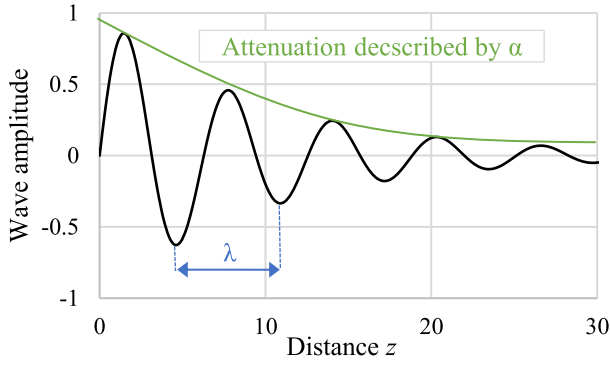


Fig. 5. Wave propagation visualization in lossy material.

skin effect are dependent on the size and shape of the core as well as on the wave frequency.

The propagation speed is related to the wavelength and frequency. Wave number  $k$  combines wavelength, frequency and the material characteristics as follows:

$$k = \frac{2\pi}{\lambda} = \frac{2\pi}{\frac{1}{f\sqrt{\mu\epsilon}}} = 2\pi f \sqrt{\mu\epsilon} = \omega\sqrt{\mu\epsilon} \quad (3)$$

where  $\omega$  is the electrical angular frequency.

Material properties used for electromagnetic wave propagation analysis must be complete. Complex permeability and permittivity in the considered materials should provide all the necessary information. The imaginary parts of the permeability and permittivity describe the material losses, while the real parts of the permeability and permittivity capture the capability to store reactive energy. As both parameters  $\bar{\mu}$  and  $\bar{\epsilon}$  are complex, wave number  $\bar{k}$  is also complex

$$\bar{k} = \omega \sqrt{\bar{\mu}\bar{\epsilon}} = \omega \sqrt{(\mu' - j\mu'')(\epsilon' - j\epsilon'')} = \beta - j\alpha \quad (4)$$

where  $\alpha$  and  $\beta$  are the attenuation and phase constants, respectively, and  $j$  is the complex operator.

The imaginary part of the wave number is the attenuation constant  $\alpha$  and defines the rate of extinction of the wave in a medium. The real part of the wave number is a phase constant  $\beta$  and is a measure of the phase shift per unit length. The wavelength is related to the phase constant. Therefore, an expression for the real part of the complex wave number provides an equation for the wavelength as an imaginary part for skin depth. Thus, we can see that

$$\alpha = -\text{Im}[\bar{k}] = \frac{1}{\delta} \Rightarrow \delta = \frac{1}{\alpha} \quad (5)$$

$$\beta = \text{Re}[\bar{k}] = \frac{2\pi}{\lambda} \Rightarrow \lambda = \frac{2\pi}{\beta}. \quad (6)$$

The calculated half wavelengths and skin depths for the two different ferrite materials are shown in Fig. 6.

For both materials, the wavelength and skin depth are frequency dependent and they are based on the experimentally measured material parameters presented in the previous section. As can be seen, the calculated wavelength and skin depth are quite different between the presented materials, and both parameters drop as frequency increases. For 3E10, the material skin depth

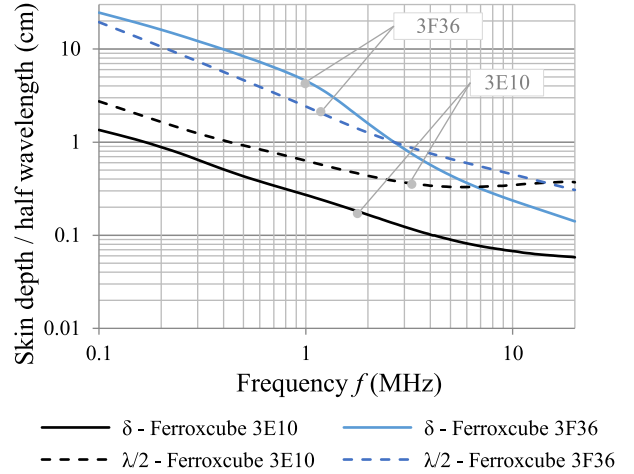


Fig. 6. Calculated half wavelength and skin depth in ferrite versus frequency.

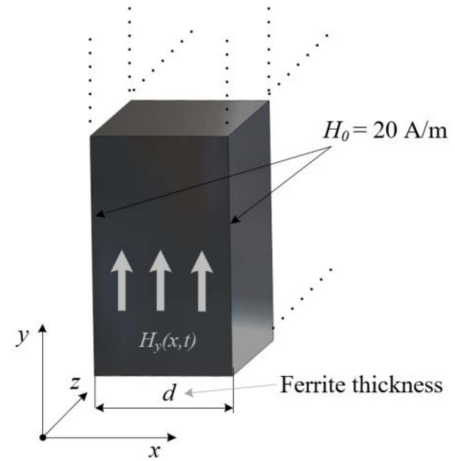


Fig. 7. Infinite ferrite plate for 1-D analytical calculation of the flux distribution in the core.

is half the half-wavelength for the frequencies in the range from 100 kHz up to 2 MHz. Thus, magnetic cores made with 3E10 are dominated by skin depth and cause a combination of magnetic and electrical losses. For 3F36 the material wave propagation and attenuation must be considered together. Below 2 MHz the skin depth is larger than half the wavelength, therefore magnetic cores with cross-sectional dimensions larger than 2 cm may be dominated by a dimensional resonance. Above 2 MHz the losses start to dominate as the skin depth frequency characteristic drops sharply below the wavelength value.

#### A. 1-D Analytical Modeling of Field Distribution

An analytical model equation has been presented in [17] for the magnetic field calculation within an infinite ferrite plate as shown in Fig. 7. The plane is infinite along the  $y$  and  $z$  axes and finite along  $x$  axis. This equation is useful in modeling the electromagnetic wave propagation of lossy materials such as ferrites. The solution of Maxwell's equations for a sinusoidal source magnetic field  $H$  of a linear, homogeneous and isotropic

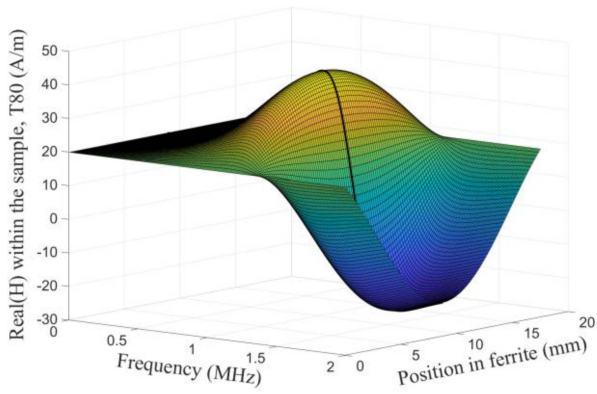


Fig. 8. 1-D model of the field distribution within infinite slab of 3F36 ferrite.

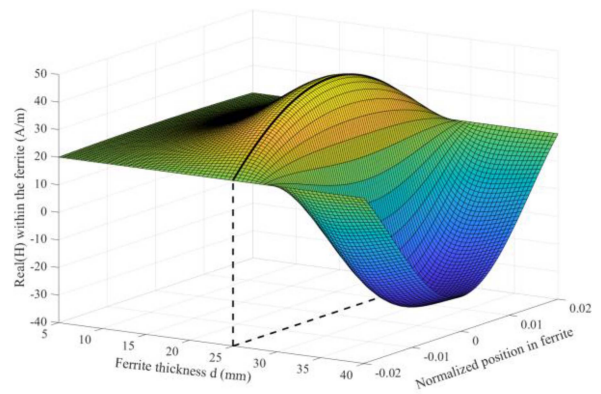


Fig. 9. 1-D calculation of the field distribution within an infinite slab of various thickness from 5 to 40 mm of 3F36 ferrite at 800 kHz.

material yields the following expression:

$$\overline{H}_y(x) = H_0 \frac{\cos\left(\frac{j\bar{k}x}{c}\right)}{\cos\left(\frac{j\bar{k}d}{2c}\right)} \quad (7)$$

where  $d$  is the ferrite thickness,  $k$  is the complex wave propagation constant,  $c$  is the speed of the light in a vacuum, and  $H_0$  is the boundary-condition value of the magnetic field on the two infinite surfaces of the ferrite plate.

The calculated magnetic field for 3F36 material in an infinite ferrite plate with a thickness of 17.5 mm, which correlates to the T80 core dimension, and an exciting field of 20 A/m is shown in Fig. 8. The magnetic field within the 3F36 ferrite core is uniform and in phase with the exciting field at low frequencies. At approximately 1 MHz there is a noticeable peak in the magnetic field. As frequency increases, the attenuation dominates and the magnetic field drops sharply. The flux density  $B(x)$  and the permeability of the core in the analyzed core plate both correlate to  $H(x)$  in the figures. Core losses are modeled by the complex permeability and permittivity. Therefore, the magnitude of the flux density at any point in the core is the result of an in-phase real part and out-of-phase imaginary part.

In the second step, the analytical equation was used to calculate the magnetic field of the 3F36 ferrite plate with varying thickness of  $d$  from 5 to 40 mm at a constant frequency of 800 kHz. The magnetic field distribution is shown in Fig. 9. The plots indicate that for a certain core size and frequency, a dimensional resonance is established. To maximize the effect of the 3F36 material permeability in a real application operating at 800 kHz, the core cross section dimension should not exceed 25 mm, where there is a noticeable peak in the magnetic field.

The calculated frequency dependency of the magnetic field for 3E10 material in an infinite ferrite plate with a thickness of 17.5 mm and an exciting field of 20 A/m is shown in Fig. 10, while the calculated magnetic field of the ferrite plate with varying thickness is shown in Fig. 11. The magnetic field within the 3E10 ferrite core is decreasing gradually as frequency increases. The skin effect is visible at low and high frequencies. At high frequency, the magnetic field is concentrated more around the outer core surface and is weakening in the core center. Analytical

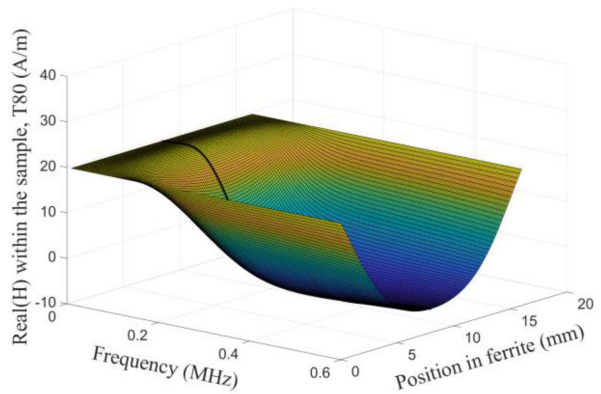


Fig. 10. 1-D model of the field distribution within infinite slab of 3E10 ferrite.

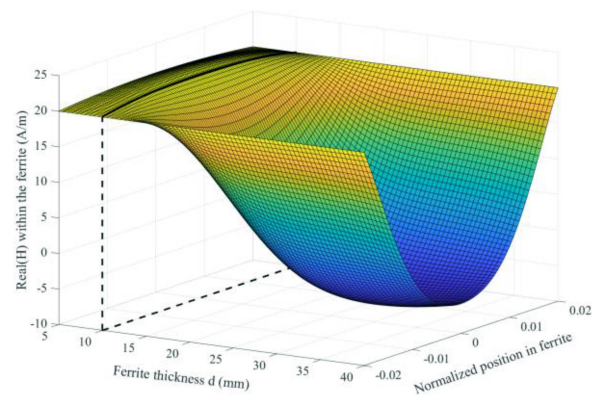
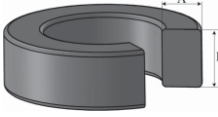


Fig. 11. 1-D calculation of the field distribution within an infinite slab of various thickness from 5 to 40 mm of 3E10 ferrite at 400 kHz.

results for 3E10 ferrite look similar to classical high-frequency current distribution in a rectangular conductor. The peak of the 3E10 material permeability at 400 kHz is visible with the core cross-section dimension equal to 10 mm.

TABLE I  
TESTED CORE PARAMETERS

Parameter	Unit	T29	T50	T80
Dimensions OD x ID x H	mm	29x19x10.5	50x30x14	80x45x17.5
Core cross section	mm <sup>2</sup>	53	140	306
Core cross section dimensions A x B	mm	5x10.5	10x14	17.5x17.5
Core volume	cm <sup>3</sup>	3.96	17.59	60.13
Core material	-	3F36/3E10	3F36/3E10	3F36/3E10
Core view	-			

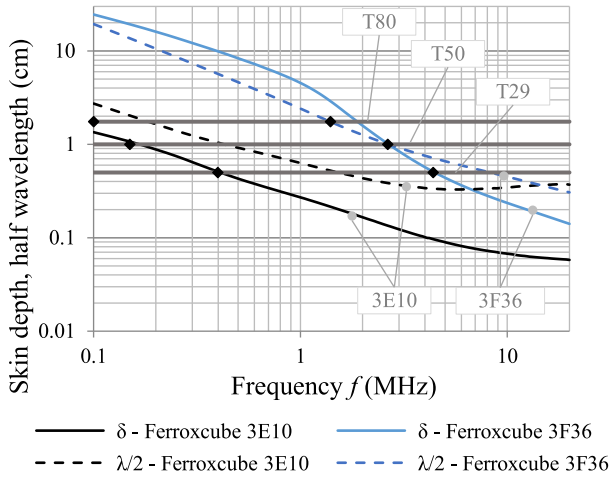


Fig. 12. Calculated half wavelength and skin depth in ferrite Versus frequency.

### B. Comparison of Experimental Versus 1-D Model Permeability Frequency Characteristic

The core size and operating frequency have a strong impact on the magnetic flux distribution. In order to show this dependency we compare three core sizes, T29, T50, and T80 of outer diameter 29, 50, and 80 mm, respectively, made of two materials 3F36 and 3E10. Detailed core dimensions are presented in Table I.

The calculated skin depths and wavelengths for both materials, as a function of frequency, with the smallest cross-sectional dimension of each tested core indicated on the graph, are shown in Fig. 12. The solid straight lines represents the smallest cross-sectional dimension of each core. The intersection of the straight line and the skin depth or half wavelength curves indicates which effect occurs first. If the frequency during the measurement is higher than 1.4 MHz for the T80 core, and 2.6 MHz for the T50 core, the measured 3F36 material real permeability shall be dominated by the dimensional resonance as the smallest cross-sectional dimensions are equal to half a wavelength, while the skin depth proves insignificant. For the T29 core, made of 3F36, the core skin depth impacts at about 4.3 MHz. The skin depth is smaller than half a wavelength, however, the difference between both parameters is small. Therefore, skin depth and

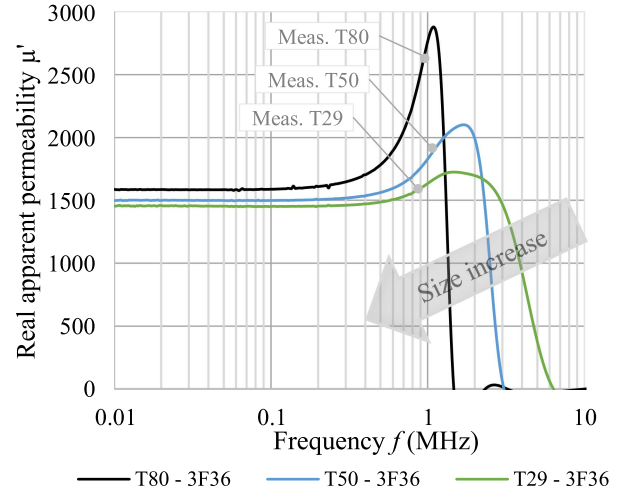


Fig. 13. Real apparent permeability versus frequency for 3F36 material based on experimental data.

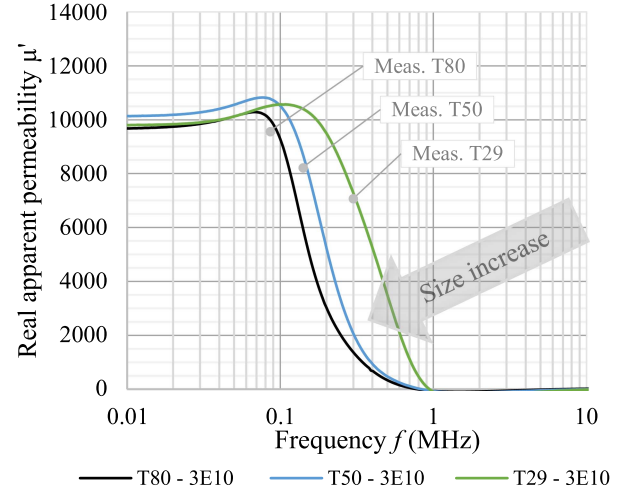


Fig. 14. Real apparent permeability versus frequency for 3E10 material based on experimental data.

dimensional resonance are impacting the core performance at the higher frequencies.

For all cores made of 3E10 skin effects will dominate the measured material properties as skin depth is significantly lower than half a wavelength.

Plots of real permeability as a function of frequency for various core sizes are shown in Figs. 13 and 14. Detail equations and procedure how to extract complex apparent permeability from (7) is explained in [17]. The cores with an external diameter of approx. 80 mm exhibit a significant change of permeability at low frequencies. As can be seen, the largest core with an external diameter of approx. 80 mm made of 3F36 material is characterized by the highest permeability peak visible at 1 MHz, followed by a sharp drop to zero at a frequency of approx. 1.5 MHz. For the same core size, but made of 3E10 material, the real permeability starts to slowly decrease at 80 kHz, and drops to zero at a frequency of approx. 600 kHz.

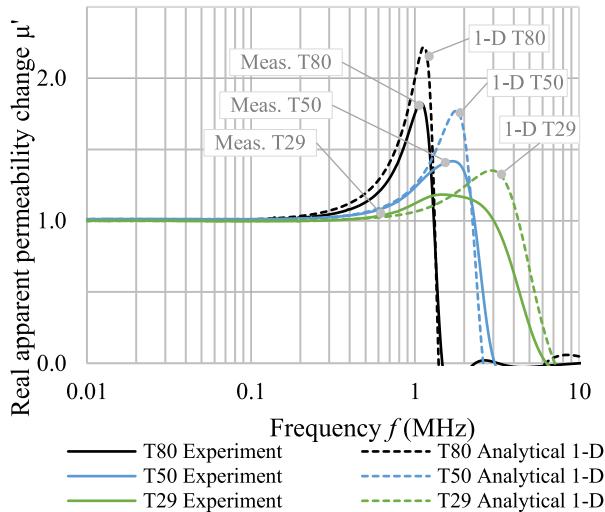


Fig. 15. Calculated and measured normalized real apparent permeability versus frequency for 3F36 ferrite.

The measured real permeability for various core sizes made with 3F36 material is constant up to about 300 kHz. For higher frequencies, the permeability peak is visible followed by a sharp drop. The permeability peak frequency depends on core size, and is visible at 1.1 MHz for the T80 core, 1.8 MHz for the T50 core and 2.1 MHz for the T29. The highest peak value of permeability is recorded for the largest core.

The real permeability characteristics for various core sizes made with 3E10 material are stable up to about 70 kHz and then are slowly decreasing. Core size impact in 3E10 is noticeable within the permeability drop for the bigger cores. However, the permeability dependence on core size is less than for the 3F36 material.

As a next step, the 1-D analytical equation was used to calculate the magnetic field for an infinite ferrite plate with the thickness corresponding to the lowest cross-sectional dimension of the tested cores, as given in bold in Table I. In order to compare the achieved results the permeability for each sample is normalized with respect to the initial permeability. The normalized real magnetic field change in the ferrite plate along the center line is compared with the normalized measured real permeability. Generated real permeability frequency characteristics for 3F36 and 3E10 cores are shown in Figs. 15 and 16, respectively.

Appendix I presents the calculated and experimental permeability values and the related errors for the various models.

The 1-D analytical equation, based on the complex material characteristics, is very accurate for both materials from low to medium frequency. The peak frequency characteristic is well represented with peak frequency errors of 3.91% and 24.6% for the 3F36 and 3E10 T80 cores, respectively. The peak permeability error is 21.4% and 6.65% for the 3F36 and 3E10 T80 cores, respectively. The best overall accuracy is achieved for the biggest core, T80, while the worst is for the T29 core, for both materials. The T80 cores have a square core cross-sectional area, therefore the smallest core cross-sectional dimension used for the magnetic field calculation is the same in both directions and

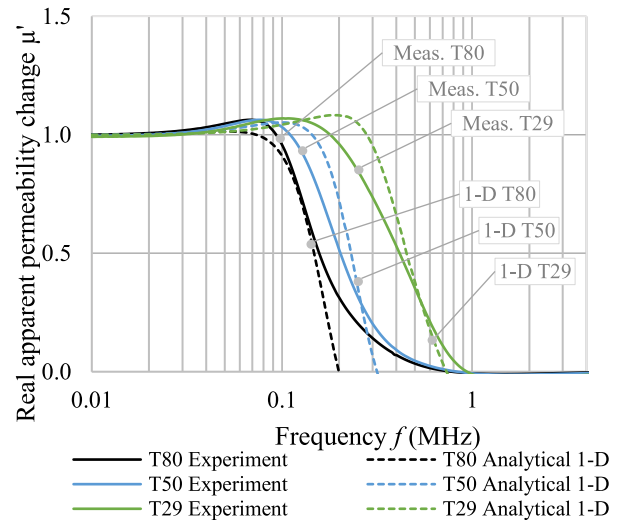


Fig. 16. Calculated and measured normalized real apparent permeability versus frequency for 3E10 ferrite.

represents a complete field distribution within the core. The T29 core results are poor due to the core cross-sectional area shape ratio of 2:1. In the case of the T29 core, the thickness of the ferrite plate was set to 5 mm, while in the other direction, the core height is 10 mm, and so, the field distributions are different. The 1-D model works best for a 1:1 core shape ratio. The T50 core with its 1.4:1 shape ratio has results in between those for the T29 and T80 cores.

As shown in Figs. 9 to 16, the core size impacts on the permeability. The nonuniform magnetic field distribution within the core can lead to local magnetic saturation, reduced permeability and substantially higher core losses. These are fundamental issues that have direct impacts on a compact and efficient magnetic component design.

#### IV. FLUX DISTRIBUTION BASED ON CORE TRANSMISSION-LINE MODEL

TLMs), with multiple variants have been developed for modeling high-frequency eddy-current effects modeling in power transformers [18], [19], [20], and wave propagation modeling in cables or machine windings [21], [22]. However, there has been limited application to model ferrite cores [23]. The principle approach is based on sectioning a magnetic core as shown in Fig. 17, while existing methods describe the core as a bulk [24], [25], [26].

The core circuit transmission line model is especially intuitive to electrical engineers. The calculation can be applied in any circuit simulator and also easily incorporated into the simulation of a higher order system. Small enough concentric shells can precisely reproduce unequal magnetic flux distributions due to the core skin and dimensional-resonance effects. The elements are modeled with a network of series inductance  $L_{1-n}$  and resistance  $R_{1-n}$  per shell with shunt capacitance  $C_{2-n}$  and resistance  $R_{2-n}$ . The RLRC network is combined into the lumped section of the transmission line, as shown in Fig. 18.



Fig. 17. Magnetic core conceptually divided into five concentric shells.

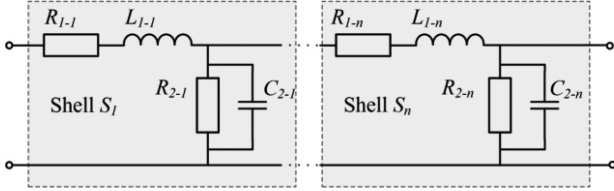


Fig. 18. Schematic of the core transmission line model.

The TLM parameters are related to the core geometry as follows:

$$L_0 = \frac{\mu_0 N^2 A_c}{l_c} \quad (8)$$

$$R_{1-n} = \mu'' L_0 \omega \left( \frac{A_{sn}}{A_c} \right) \quad (9)$$

$$L_{1-n} = \mu' L_0 \left( \frac{A_{sn}}{A_c} \right) \quad (10)$$

$$R_{2-n} = \frac{l_s}{\varepsilon'' \varepsilon_0 \omega l_c \Delta x} \quad (11)$$

$$C_{2-n} = \frac{\varepsilon' \varepsilon_0 l_c \Delta x}{l_s} \quad (12)$$

where  $A_S$  is the cross-sectional area of the each shell,  $A_C$  is the entire core cross section,  $l_S$  is the shell mean path length,  $l_C$  is the magnetic core path length,  $n$  is the shell number,  $\Delta x$  is the shell thickness, and  $N$  is the number of turns, which we take as 1 for the model of a core.

The TLM uses a magnetic core modeled by concentric shells. The number of shells is related to the model accuracy: the higher the number of shells, the better the calculation accuracy. The TLM accuracy for a T50 core of 3F36 material at a frequency range up to 10 MHz for various number of shells is shown in Fig. 19.

The number-of-shells effect on calculated permeability is shown in Fig. 19, while an average relative error is shown in Fig. 20. The average error is calculated with reference to the permeability characteristic calculated for 50 shells. Each material and core size required an individual approach to the shell number selection, and the number of shells is increased until the defined average error is achieved.

The TLM is used to calculate the frequency-dependent permeability characteristics for the cores given in Table I. The apparent permeability of the core is calculated based on the simulated

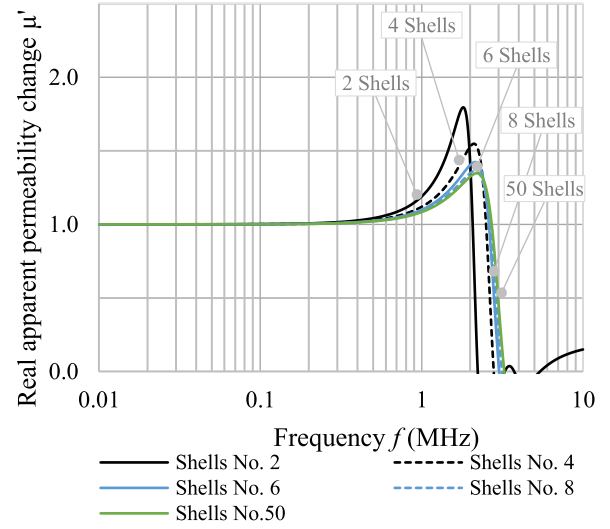


Fig. 19. Calculated normalized real apparent permeability versus frequency for T50 3F36 ferrite core for variable shell numbers.

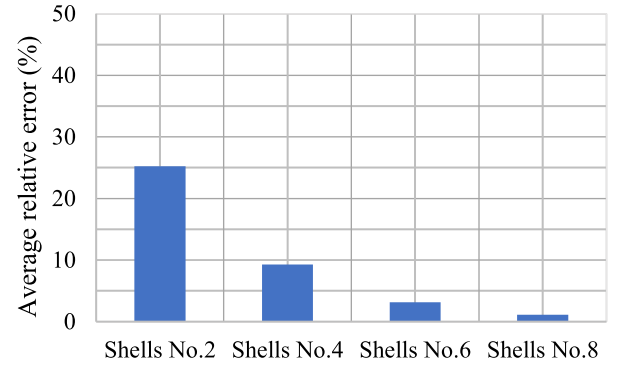


Fig. 20. Average relative error vs. shell number for 3F36 T50 ferrite core.

impedance at the input of transmission line model. Each magnetic core was arbitrarily divided into eight concentric shells. The achieved normalized real permeability characteristics were compared with the normalized measured real permeability characteristic. The permeability for each sample is normalized in relation to its permeability at 10 kHz. The plotted frequency characteristic for both materials, are shown in Figs. 21 and 22, for 3E10 and 3F36, respectively.

Appendix I Table AI presents the data for TLM model.

The core TLM based on the complex material characteristics correlates well with the measured characteristics. The best accuracy is achieved for the biggest core, i.e., the T80 made of 3E10 material. For the 3F36 material the best fits of the real permeability characteristic were achieved for the T50 core.

As is often the case in modelling, errors could be reduced in the TLM model by using nonlinear elements in the model. Additionally, the actual paths of the displacement and conduction currents are closer to circular towards the center of the core and are more rectangular toward the outside. The TLM model is based on rectangular shells for simplicity. Thus, this is not an exact model, even with a large number of shells. There is also uncertainty in the characteristics of the material, as with all the modeling methods.



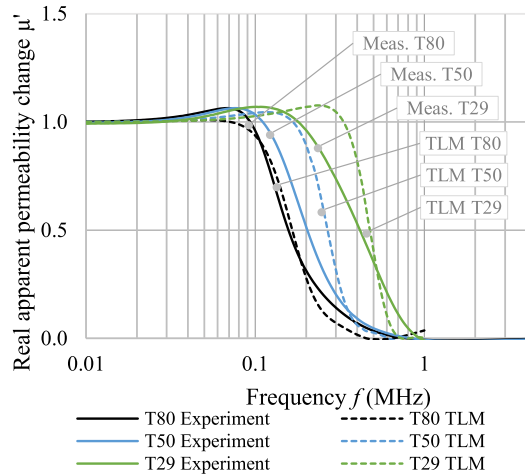


Fig. 21. Calculated and measured normalized real apparent permeability versus frequency for 3E10 ferrite.

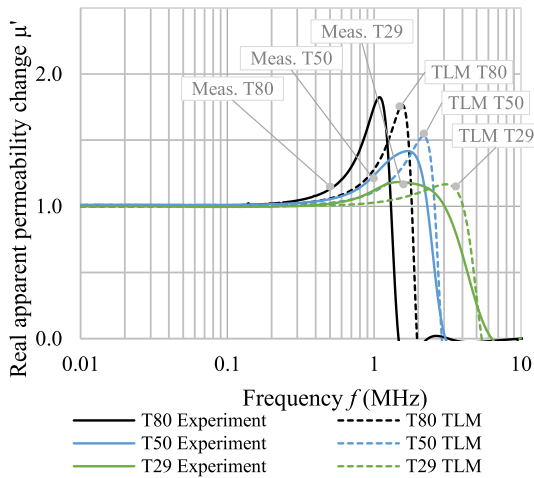


Fig. 22. Calculated and measured normalized real apparent permeability versus frequency for 3F36 ferrite.

## V. FLUX DISTRIBUTION BASED ON FEA MODELING

The permeability vs. frequency characteristic does not provide detailed information on the flux distribution in a ferrite core. The finite-element method (FEM) enables us to visualize the flux distribution in the core. An analysis is performed using the Ansys software Maxwell 3-D and eddy-current solver. The mesh size was individually defined for each frequency point to minimize the energy error ( $<0.5\%$ ). The model of each toroidal core was created based on the geometrical data given in Table I. Eddy current solver is a full wave solution that includes electromagnetic wave radiation effects. The first pair of simulations, are shown in Fig. 23(a) and (b) for 30 and 300 kHz, respectively. At the low frequency of 30 kHz the reluctance effect is clearly visible in the core. At the high frequency of 300 kHz the frequency effects start to dominate. At the higher frequency the magnetic flux density distribution has an analogy to the current distribution in a conductor. The magnetic flux is concentrated in the outer circumference while the core center exhibits flux density weakening. In the inner core part the magnetic flux flows in an opposite direction.

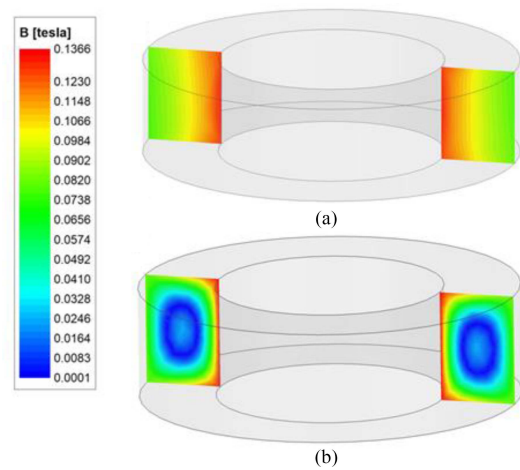


Fig. 23. FEA results of magnetic RMS flux distribution in the T50 ferrite core at (a) 30 kHz and (b) 300 kHz – material 3E10.

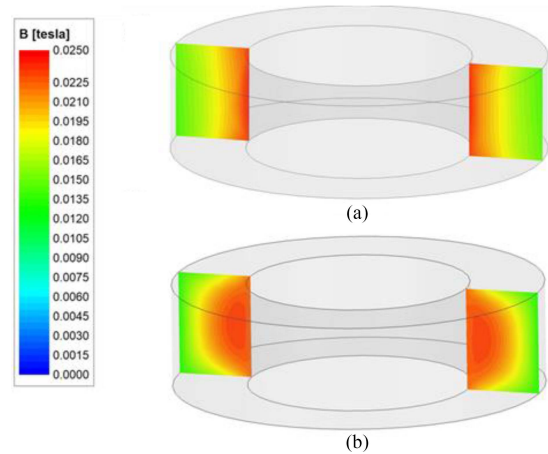


Fig. 24. FEA results of magnetic RMS flux distribution in the T50 ferrite core at (a) 30 kHz and (b) 1.7 MHz – material 3F36.

In the second simulation 3F36 material is selected, and the magnetic flux distributions at 30 kHz and 1.7 MHz are shown in Fig. 24(a) and (b) respectively. At the high frequency, a large amplitude flux is concentrated in the inner part of the core cross section for the 3F36 material, which is an effect of the dimensional resonance.

The normalized real values of the resultant simulated magnetic permeability characteristic are compared with the normalized experimentally-determined real permeability characteristic. The plotted frequency characteristic for both materials are shown in the Figs. 25 and 26, for 3E10 and 3F36, respectively.

Appendix I Table AI presents the data for the FEM model.

As can be seen from the plots, the simulated real permeability follows the measurements. An exact match is achieved at low frequencies. Discrepancies in the characteristics emerge at high frequencies. The simulated complex characteristic, regardless of material and core size, decreases as the high frequency increases. It is possible that an improvement may be achieved if the simulation software is changed from Maxwell 3-D to HFSS, as it is the frequency range where the wave effects, better utilized with HFSS, may dominate the flux distribution.

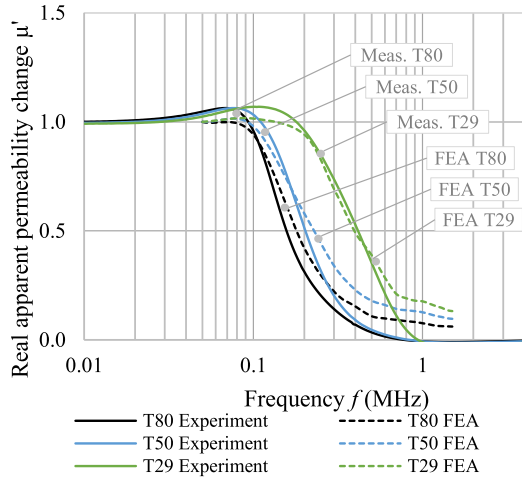


Fig. 25. FEA simulated and measured normalized real apparent permeability versus frequency for 3E10 ferrite.

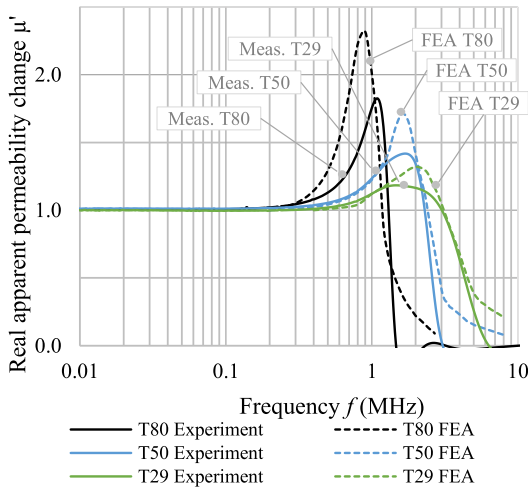


Fig. 26. FEA simulated and measured normalized real apparent permeability versus frequency for 3F36 ferrite.

## VI. FLUX DISTRIBUTION EXPERIMENTAL VALIDATION

Two T80 ferrite cores are selected to validate the analytical calculations and FEM results of flux distribution. In order to measure the magnetic flux, three sets of bores were made in the each selected core. One set of bores consists of two vertical bores and one horizontal bore of 0.75 mm diameter each. The measurement system setup and windings arrangement are presented in Fig. 27.

The procedure for calculation of the magnetic flux in the core is discussed in detail in [10] and is briefly outlined here. The sense windings are inserted into the bored holes to determine the flux and the phase shift of each core segment.

An example of how the flux in section  $S_D$  is calculated is presented below. As many as four steps are needed to determine the flux density in section  $S_D$ . In the first and the second steps, voltage  $V_1$  for sections  $S_1$  and  $S_D$ , and voltage  $V_2$  for section  $S_2$  are successively measured using the core configuration shown in Fig. 28.

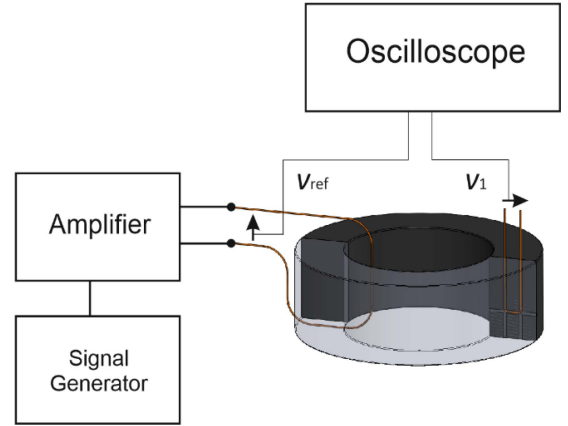


Fig. 27. Measurement setup for magnetic flux distribution validation.

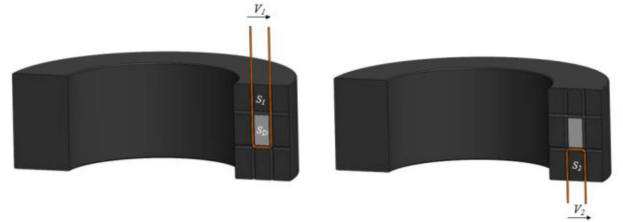


Fig. 28. Winding configuration to measure voltage  $V_1$  and  $V_2$ .

In the third step, the voltage  $V_D$  corresponding to section  $S_D$  is achieved by subtracting  $V_2$  from  $V_1$

$$V_D = V_1 - V_2 = V_{1M} \sin(\omega t + \varphi_1) - V_{2M} \sin(\omega t + \varphi_2) \quad (13)$$

where  $V_{1M}$  and  $V_{2M}$  are the maximum value of  $V_1$  and  $V_2$ , respectively, and  $\varphi_1$  and  $\varphi_2$  are the phases of  $V_1$  and  $V_2$ , respectively.

In the final step, the magnetic flux  $\Phi_D$  in section  $S_D$  is calculated as a function of the sinusoidal voltage and frequency for  $N = 1$  as follows:

$$\Phi_D = A_D \cdot B_D = A_D \frac{V_D}{2\pi f A_D} = \frac{V_D}{2\pi f} \quad (14)$$

where  $A_D$  is the  $S_D$  cross-sectional area, and  $B_D$  is the magnetic flux density corresponding to section  $S_D$ .

The excitation voltage is changed for different frequencies. The flux density is normalized by dividing by the main flux density at each frequency

$$\text{Magnetic flux density ratio } (f) = \frac{B_D(f)}{B_{CORE}(f)} \quad (15)$$

where  $B_{CORE}$  is the magnetic flux density of the core.

The data acquired during the experimental tests allow us to determine the flux in the four sections of the core as shown in Fig. 29.

The normalized magnetic flux density distributions in each section of the T80 core, made with 3E10, are shown in Fig. 30. The magnetic flux is concentrated in the outer part of the core while the core center exhibits flux density weakening. Note that

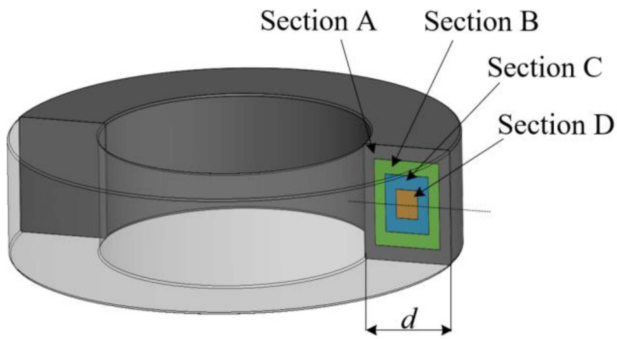


Fig. 29. Section arrangement in tested ring core.

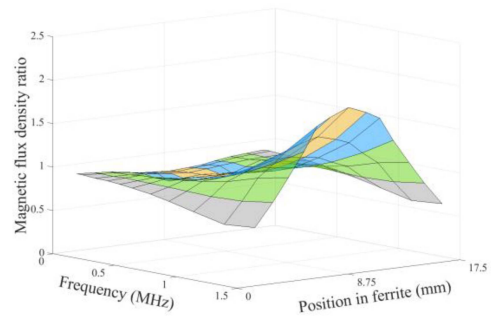


Fig. 32. Experimental magnetic flux density ratio in the each segment, frequency characteristic—material 3F36.

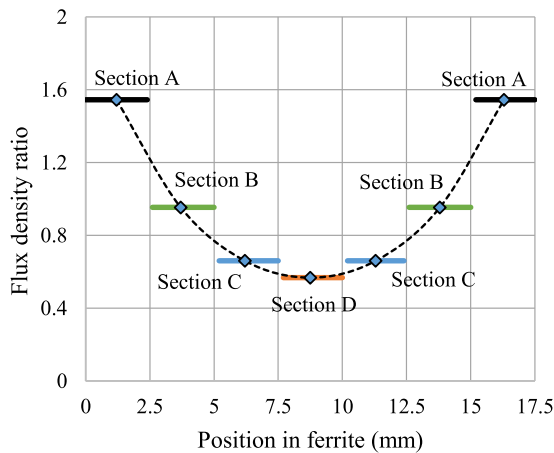


Fig. 30. Experimental magnetic flux density ratio in the each segment of tested core at 300 kHz—material 3E10.

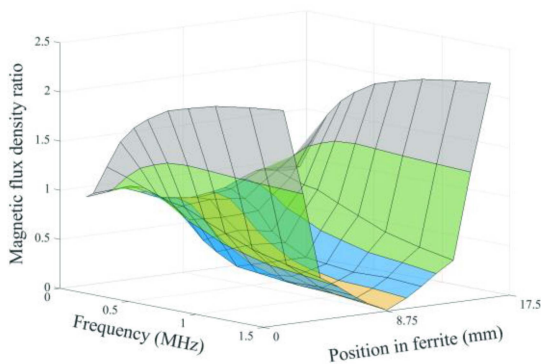


Fig. 31. Experimental magnetic flux density ratio in the each segment, frequency characteristic—material 3E10.

the measurements show the averaged flux density for the section, and so the reluctance effect is not shown.

As a next step, the magnetic flux distribution is presented for the frequency range of 50 kHz to 1.5 MHz. The obtained results allow us to present the magnetic flux density change as shown in Figs. 31 and in 32 for 3E10 and 3F36 materials, respectively. The 3E10 material is more subject to the core skin effect, which results in a frequency-dependent nonuniform flux distribution.

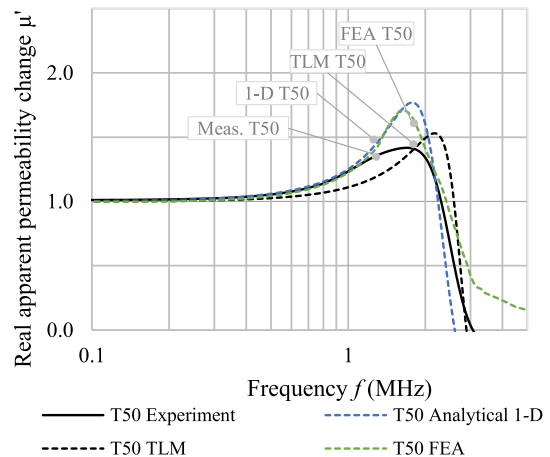


Fig. 33. Calculated and measured normalized real apparent permeability versus frequency for 3F36, T50 ferrite core.

For the three internal sections, the flux decreases together with the frequency. For outer Section VI-A, the flux increases along with frequency. For the 3F36 material, the operating frequency, where flux distribution in the core is constant, is extended up to 900 kHz. At the higher frequencies for the three internal sections, the flux increases together with the frequency, while for the outer section there is a decrease. The experimental results confirm qualitatively the analytical calculations and the FEM analysis. The magnetic flux is concentrated in the outer circumference while the core center exhibits flux density weakening. Magnetic cores made of 3E10 are dominated by the skin depth caused by the combination of high magnetic and electrical losses. For the 3F36 cores the flux is stronger and concentrated in the inner part of the core cross section. For the 3F36 material in the considered frequency range, the flux distribution is dominated by dimensional resonance.

### VII. COMPARISON OF EXPERIMENTAL AND ANALYTICAL APPROACHES

The three presented methods for magnetic flux analysis, based on the 1-D analytical equation, the circuit TLM and the FEM compare well with the measurements. Frequency characteristics for the T50 core of 3F36 material are shown in Fig.33. The calculated permeability characteristics based on the 1-D

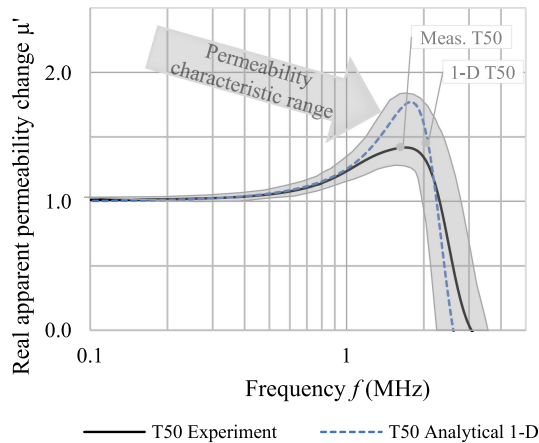


Fig. 34. Calculated and measured normalized real apparent permeability versus frequency for 3F36, T50 ferrite core.

TABLE II  
CPU TIMES FOR CALCULATION OF THE T50, 3F36 FERRITE CORE REAL PERMEABILITY CHARACTERISTICS

Analysis type	Number of points on characteristic	Calculation time
1-D analytical	800	5.1 s
TLM	800	3.8 s
FEM	18	43.5 h

analytical equation and the FEA method show permeability peaks at the same frequency as the measurements. However, the calculated permeability is about 30% higher than measured. The calculated permeability characteristic based on the TLM is shifted in relation to the measurement at the low-frequency region, but has the best correlation at high frequency.

The selection of the right model by comparing with measurements is challenging. Input data for each model is a dataset of ferrite frequency characteristic based on complex permeability and permittivity. By the nature of the magnetic material, complex permeability and permittivity parameters may vary with a tolerance of  $\pm 20\%$ . Fig. 34 shows the tolerance envelope calculated with the analytical model. The envelope outlines the absolute worst case of all possible combinations of the material parameters without factoring in the probability of the occurrence. The measured characteristic is within the envelope, therefore the 1-D model may be considered as a good indicator of the high-frequency effects in the ferrite core.

One additional aspect of the methods discussed is the calculation time. As an example, Table II gives the calculation time necessary to generate the real permeability characteristic for the T50 3F36 core. The basis of the comparison is a workstation equipped with Intel Xeon W-2133 3.6 2666 MHz 6C CPU 64 GB DDR4. The calculation time is the lowest for the TLM method at 3.8 s and far higher for the FEM method. Almost two days are needed for a single FEM calculation!

## VIII. CONCLUSION

The magnetic component design is key to a successful EMI filter. High-frequency effects, such as the skin effect and the dimensional resonance are often the limiting factor for high-power EMI filters. The high-frequency effects are likely to render the classical design approach inefficient, leading to an oversized EMI filter and ultimately a higher cost. Therefore, the analysis and the identification of the core high-frequency effects used in high-quality modelling are of primary importance for successful CMC design.

In order to design magnetic components for high frequency applications, much more detailed information on magnetic materials is required. Detailed experimental parameters are presented and used in the development of analytical models. The materials' complex permeability and permittivity are key parameters for the EMC filter design process as they directly impact the power loss and inductance.

High-frequency effects such as dimensional resonance and skin effect within the core can be modelled and predicted based on the discussed models. The models are used to investigate skin depth and dimensional resonance, and the clear impact of these phenomena can be observed for the various materials. The presented methods show a very good correlation with the measurements.

The nonuniform magnetic flux distribution has been experimentally validated for two Mn-Zn materials: 3F36 and 3E10. It is observed that in a high-permeability material, such as 3E10, the magnetic flux undergoes a skin effect that is analogous to that in ohmic conductors. At high frequency, the magnetic flux in the core's middle sections may flow in an opposite direction to the equivalent flux in the core. Lower permeability materials, such as 3F36, show a magnetic flux increase in the core's middle section caused by the wave propagation effects of a dimensional resonance.

The validated models correlate well to the experimental results, and thus can contribute to a speedy design process.

## APPENDIX I

Four simple types of errors are now calculated to assess the quality of the each discussed models, as given in Table A.I. The first error is calculated by comparing the calculated and experimental permeabilities at 10 kHz. The second error is calculated by comparing the modeled and experimental permeabilities at 500 kHz for 3F36 and 50 kHz for 3E10, frequencies where we see the high-frequency effects beginning to impact. The third error compares the peak permeability values. The fourth error is calculated by comparing the modeled and experimental frequencies at peak permeability.

## APPENDIX II

In order to reproduce the measured ferrite complex permeability and permittivity characteristics, data for tested materials are presented in Table A.II and Table A.III, respectively.

TABLE AI  
MODEL ERRORS

	Material	T80	T50	T29	T80	T50	T29	T80	T50	T29
		1-D analytic model			TLM model			FEA model		
Calculated permeability at 10 kHz	3F36	1593	1592	1587	1593	1696	1638	1603	1610	1586
Measured permeability at 10 kHz	3F36	1600	1600	1600	1600	1600	1600	1600	1600	1600
Error at 10 kHz	3F36	-0.40 %	-0.50 %	-0.80 %	-0.44 %	1.97 %	2.39 %	0.20 %	0.60 %	-0.90 %
Calculated permeability at 500 kHz	3F36	1925	1701	1628	1691	1742	1650	2069	1667	1792
Measured permeability at 500 kHz	3F36	1814	1689	1632	1814	1689	1632	1814	1689	1632
Error at 500 kHz	3F36	6.14 %	0.73 %	-0.29 %	-6.74 %	3.15 %	1.09 %	14.1 %	-1.28 %	9.77 %
Calculated permeability at peak	3F36	3544	2832	2163	2813	2594	1911	3712	2736	2112
Measured permeability at peak	3F36	2918	2268	1894	2918	2268	1894	2918	2268	1894
Error at peak	3F36	21.4 %	24.8 %	14.2 %	-3.59 %	14.3 %	0.94 %	27.2 %	20.6 %	11.5 %
Calculated peak frequency (MHz)	3F36	1.114	1.767	2.821	1.562	2.113	3.214	0.900	1.600	2.000
Measured peak frequency (MHz)	3F36	1.072	1.725	2.095	1.072	1.725	2.095	1.072	1.725	2.095
Frequency error at peak	3F36	3.91 %	2.43 %	34.6 %	45.7 %	22.4 %	53.4 %	16.1 %	7.24 %	4.53 %
Calculated permeability at 10 kHz	3E10	10006	9957	9917	9990	10040	10080	10030	9950	9940
Measured permeability at 10 kHz	3E10	10000	10000	10000	10000	10000	10000	10000	10000	10000
Error at 10 kHz	3E10	0.06 %	-0.43 %	-0.83 %	-0.10 %	0.40 %	0.80 %	0.30 %	-0.50 %	-0.60 %
Calculated permeability at 50 kHz	3E10	10133	10217	10121	10080	10159	10081	10120	10010	9960
Measured permeability at 50 kHz	3E10	10478	10381	10253	10478	10381	10253	10478	10381	10253
Error at 50 kHz	3E10	-3.29 %	-1.58 %	-1.29 %	-3.79 %	-2.13 %	-1.67 %	-3.41 %	-3.57 %	-2.85 %
Calculated permeability at peak	3E10	10137	10523	10830	10080	10446	10759	10150	10090	10040
Measured permeability at peak	3E10	10633	10640	10693	10633	10640	10693	10633	10640	10693
Error at peak	3E10	-4.65 %	-1.09 %	1.28 %	-5.19 %	-1.82 %	0.61 %	-4.53 %	-5.16 %	-6.10 %
Calculated peak frequency (kHz)	3E10	52.180	99.320	183.63	54.661	111.72	235.78	60.000	70.000	125.00
Measured peak frequency (kHz)	3E10	69.218	78.760	112.34	69.218	78.760	112.34	69.218	78.760	112.34
Frequency error at peak	3E10	24.6 %	26.1 %	63.4 %	21.0 %	41.8 %	109 %	13.3 %	11.1 %	11.2 %

TABLE AII  
REAL AND IMAGINARY PERMITTIVITY CHARACTERISTICS

Frequency (MHz)	Ferroxcube 3E10		Ferroxcube 3F36	
	$\epsilon'$	$\epsilon''$	$\epsilon'$	$\epsilon''$
0.01	218962	3292135	61262	76243
0.1	85011	814288	36788	18587
0.2	81232	413498	32208	13651
0.3	77352	289593	29893	11600
0.4	74238	220139	28382	10426
0.5	71206	180479	27275	9645
0.6	68758	156171	26410	9080
0.7	66158	135719	25703	8646
0.8	64065	122039	25109	8299
0.9	62211	111676	24598	8013
1.0	60678	103988	24151	7773
2.5	44943	56722	20622	6134
5.0	33149	39108	18321	5250
7.5	27023	32489	17081	4842
10.0	22925	28670	16284	4576
12.5	19845	26035	15679	4384
15.0	17632	24247	15202	4236
17.5	15747	22909	14810	4116
20.0	14282	21537	14484	4018

TABLE AIII  
REAL AND IMAGINARY PERMEABILITY CHARACTERISTIC

Frequency (MHz)	Ferroxcube 3E10		Ferroxcube 3F36	
	$\mu'$	$\mu''$	$\mu'$	$\mu''$
0.01	9812	228	1482	8
0.1	10215	621	1479	11.2
0.2	10150	2020	1478	9.8
0.3	9542	3230	1480	10.3
0.4	8529	4032	1483	10.5
0.5	7475	4375	1488	13.1
0.6	6659	4418	1499	13.7
0.7	6024	4349	1509	16.7
0.8	5549	4251	1522	20.4
0.9	5207	4156	1537	25.6
1.0	4806	4025	1561	38.2
2.5	2532	3264	1561	503
5.0	1060	2400	1078	763
7.5	524	1776	785	728
10.0	297	1315	606	650
12.5	222	1052	513	593
15.0	173	831	445	545
17.5	161	716	392	508
20.0	155	596	342	471

ACKNOWLEDGMENT

We would like to offer special thanks to Edward Herbert for his valuable and constructive suggestions during planning and development of this article.

REFERENCES

[1] E. Hoene, G. Deboy, C.R. Sullivan, and G. Hurley, "Outlook on developments in power devices and integration: Recent investigations and future requirements," *IEEE Power Electron. Mag.*, vol. 5, no. 1, pp. 28–36, Mar. 2018.  
 [2] G. Hurley, T. Merkin, and M. Duffy, "The performance factor for magnetic materials revisited: The effect of core losses on the selection of core size in transformers," *IEEE Power Electron. Mag.*, vol. 5, no. 3, pp. 24–34, Sep. 2018.

[3] M.S. Ryłko, B.J. Lyons, and J.G. Hayes, "Revised magnetics performance factor and experimental comparison of high-flux materials for high-current DC-DC inductors," *IEEE Trans. Power Electron.*, vol. 26, no. 8, pp. 2112–2126, Aug. 2011.  
 [4] J. Biela, M. Schweizer, S. Waffler, B. Wrzecionko, and J.W. Kolar, "SiC vs. Si evaluation of potentials for performance improvement of power electronics converter system by SiC power semiconductors," *IEEE Trans. Ind. Electron.*, vol. 58, no. 7, pp. 2872–2882, Jul. 2011.  
 [5] G.R. Skutt, *High-Frequency Dimensional Effects in Ferrite-Core Magnetic Devices*, Ph.D. dissertation, Virginia Polytechnic Institute, Blacksburg, VA, USA, 1996.  
 [6] G.R. Skutt and F.C. Lee, "Characterization of dimensional effects in ferrite-core magnetic devices," in *Proc. IEEE Power Electron. Specialist Conf.*, 1996, pp. 1435–1440.  
 [7] P. Pengfei and Z. Ning, "Magnetodielectric effect of mn-zn ferrite at resonant frequency," *J. Magnetism Magn. Mater.*, vol. 416, pp. 256–260, Oct. 2016.

- [8] B.D Cullity and C.D. Graham, *Introduction to Magnetic Materials*, New York, NY, USA: Wiley, 2009.
- [9] M. Kaćki, M.S. Rylko, J.G Hayes, and C.R. Sullivan, "Magnetic material selection for EMI filter," in *Proc. IEEE Energy Convers. Congr. Expo.*, 2017, pp. 2350–2356.
- [10] M. Kaćki, M.S. Rylko, J.G Hayes, and C.R. Sullivan, "A study of flux distribution and impedance in solid and laminar ferrite cores," in *Proc. IEEE Appl. Power Electron. Conf. Expo.*, 2019, pp. 2681–2687.
- [11] M. Kaćki, M.S. Rylko, J.G Hayes, and C.R. Sullivan, "A practical method to define high frequency electrical properties of MnZn ferrites," in *Proc. IEEE Appl. Power Electron. Conf. Expo.*, 2020, pp. 216–222.
- [12] M. Kaćki, M.S. Rylko, and E. Herbert, "PSMA-SMA special project – phase I, investigation on magnetic flux propagation in ferrite cores," in 2018.
- [13] M. Kaćki, M.S. Rylko, and E. Herbert, "PSMA-SMA special project – phase II, investigation on magnetic flux propagation in ferrite cores," 2020.
- [14] Wayne Kerr Electronics, "Impedance analyzer datasheet." Accessed: Sep. 6, 2022. [Online]. Available: [https://www.waynekerrtest.com/products\\_detail.php?index=4&brand=Wayne%20Kerr](https://www.waynekerrtest.com/products_detail.php?index=4&brand=Wayne%20Kerr)
- [15] Ferroxcube Corporation, "Material brochure." Accessed: Sep. 6, 2022. [Online]. Available: [https://www.ferroxcube.com/en-global/download/index/material\\_brochure](https://www.ferroxcube.com/en-global/download/index/material_brochure)
- [16] E. C. Snelling, *Soft Ferrites: Properties and Applications*. 1st ed. Oxford, U.K.: Newnes-Butterworth, 1969.
- [17] F. G. Brockman, P. H. Dowling, and W. G. Steneck, "Dimensional effects resulting from a high dielectric constant found in a ferromagnetic ferrite," *Phys. Rev.*, vol. 77, no. 1, pp. 305–307, Jan. 1950.
- [18] F. de Leon and A. Semlyen, "Time domain modeling of eddy current effects for transformer transients," *IEEE Trans. Power Del.*, vol. 8, no. 1, pp. 271–280, Jan. 1993.
- [19] Ch. Zhao, J. Ruan, Z. Du, S. Liu, Y. Yu, and Y. Zhang, "Calculation of parameters in transformer winding based on the model of multi-conductor transmission line," in *Proc. Int. Conf. Elect. Mach. Syst.*, 2008, pp. 463–467.
- [20] S. M. H. Hosseini and P. R. Baravati, "New high frequency multi-conductor transmission line detailed model of transformer winding for PD study," *IEEE Trans. Dielect. Elect. Insul.*, vol. 24, no. 1, pp. 316–323, Feb. 2017.
- [21] H.D. Gersem and A. Muetze, "Finite-element supported transmission-line models for calculating high-frequency effects in machine windings," *IEEE Trans. Magn.*, vol. 48, no. 2, pp. 787–790, Feb. 2012.
- [22] O. Magdun, A. Binder, A. Rocks, and O. Henze, "Prediction of common mode ground current in motors of inverter-based drive systems," in *Proc. Int. Aegean Conf. Elect. Mach. Power Electron.*, 2007, pp. 806–811.
- [23] C. R. Sullivan, "Lumped model to explain and approximate dimensional effects in ferrite cores," in *Proc. PSMA Workshop, IEEE Appl. Power Electron. Conf.*, Mar. 2019, pp. 1–25.
- [24] Z. Lei Z.Lanyoung, L. Bing, Ch. Papavassiliou, and W. Wugui, "High-frequency modeling of common-mode chokes based in the identification of frequency parameters," in *Proc. IEEE Int. Conf. Mechatronic Automat.*, 2018, pp. 779–784.
- [25] M. Kovacic, Z. Hanic, S. Stipetic, Sh. Krishnamurthy, and D. Zarko, "Analytical wideband model of a common-mode choke," *IEEE Trans. Power Electron.*, vol. 27, no. 7, pp. 3173–3185, Jul. 2012.
- [26] K. Nomura, N. Kikuchi, Y. Watanabe, S. Inoue, and Y. Hattori, "Novel SPICE model for common mode choke including complex permeability," in *Proc. IEEE Appl. Power Electron. Conf. Expo.*, 2016, pp. 3146–3152.
- [27] M. Kaćki, M. S. Rylko, J. G. Hayes, and C. R. Sullivan, "Measurement methods for high-frequency characterizations of permeability, permittivity, and core loss of Mn-Zn ferrite cores," *IEEE Trans. Power Electron.*, vol. 37, no. 12, pp. 15152–15162, Dec. 2022.



**Marcin Kaćki** received the M.Eng.Sc. degree in electrical engineering from AGH University of Science and Technology, Kraków, Poland, in 2012. He is currently working toward the Ph.D. degree in high frequency magnetics with the University College Cork, Cork, Ireland.

In 2011, he was with R&D team in SMA Magnetics, where he is currently a Senior Engineer. His research interests include optimization and integration of the magnetic components with emphasis on EMC filters, numerical analysis and power electronics.



**Marek S. Rylko** (Member, IEEE) received the B.E. degree from the University of Bielsko-Biala, Bielsko-Biala, Poland, in 2003, the M.Eng.Sc. degree from the Silesian University of Technology, Gliwice, Poland, in 2004, and the Ph.D. degree from University College Cork (UCC), Cork, Ireland, in 2011, all in electrical engineering.

From 2005 to 2010, he was with the Power Electronics Research Laboratory, where he was involved in various industrial activities. Following this, he was with the Research Staff of dtw Sp. z o.o., Zabierzow, Poland, that was subsequently rebranded to SMA Magnetics Sp. z o.o. and he is currently heading R&D activities. His research interests include dc-dc and dc-ac converter topologies, power electronics, with emphasis on analysis, optimization, and integration of the magnetic components in power electronic converters for automotive and energy applications.



**John G. Hayes** (Senior Member, IEEE) received the B.E. degree from the University College Cork, Cork, Ireland, the M.S.E.E. degree from the University of Minnesota, Minneapolis—St. Paul, MN, USA, the M.B.A. degree from California Lutheran University, Thousand Oaks, CA, USA, and the Ph.D. degree from the University College, Cork, Ireland, in 1986, 1989, 1993, and 1998, respectively.

From 1986 to 1988, he was a Research Fellowship for power electronics under Prof. N. Mohan with the University of Minnesota. From 1988 to 1990, he was with the Power One, Inc., Camarillo, CA, USA, designing linear and switching ac-dc power converters. In 1990, he was with the General Motors Advanced Technology Vehicle (formerly Hughes Aircraft Company and Delco Electronics), Culver City, and later Torrance, CA, where he was a Design Engineer and the Technical Manager in the fields of propulsion drives and battery charging for electric vehicles, especially for heavy-duty vehicles and the General Motors EV1 electric car. From 1995 to 1997, he pursued the Ph.D. part-time as a Howard Hughes Corporate Fellow while continuing to work as a Design Engineer with GM. Subsequently, he was the Technical Manager on EV battery chargers and infrastructure. He was the Academic Staff with UCC in late 2000 and currently teaches power engineering and power electronics and drives. He directs the Power Electronics Research Laboratory, UCC. He is the lead author, with coauthor Dr. A. Goodarzi, his former GM colleague and the CEO of Magmotor, on *Electric Powertrain: Systems, Power Electronics and Drives for Electric, Hybrid and Fuel Cell Vehicles* (English-language edition, Wiley, 2018; Chinese-language edition, China Machine Press, 2021). His research interests include power electronics, machines, and magnetics for automotive, and energy applications.



**Charles R. Sullivan** (Fellow, IEEE) received the B.S. degree (with highest Hons.) in electrical engineering from Princeton University, Princeton, NJ, USA, in 1987, and the Ph.D. degree in electrical engineering from the University of California, Berkeley, CA, USA, in 1996.

Between the B.S. and Ph.D. degrees, he was with Lutron Electronics designing electronic ballasts. He is currently a Professor with the Thayer School of Engineering at Dartmouth, Hanover, NH, USA, where he is also the Director of the Power Management Integration Center. He has 43 U.S. patents and is a Co-Founder of Resonant Link, Inc. His research interests include modeling and design optimization of magnetics and other passive components for high-frequency power conversion and wireless power transfer.

Dr. Sullivan was the recipient of the Power Electronics Society Modeling and Control Technical Achievement Award, in 2018, and three Power Electronic Society Prize Paper Awards.